Improved heralded single-photon source with a photon-number-resolving superconducting nanowire detector

SAMANTHA I. DAVIS[1,2], ANDREW MUELLER[2,3], RAJU VALIVARTHI[1,2], NIKOLAI LAUK[1,2], LAUTARO NARVAEZ[1,2], BORIS KORZH[4], ANDREW D. BEYER[4], MARCO COLANGELO[5], KARL K. BERGGREN[5], MATTHEW D. SHAW[4], SI XIE[1,2,7], NEIL SINCLAIR[1,2,6], AND MARIA SPIROPULU[1,2,*]

[1] Division of Physics, Mathematics and Astronomy, California Institute of Technology, 1200 E California Blvd., Pasadena, CA 91125, USA
[2] Alliance for Quantum Technologies (AQT), California Institute of Technology, 1200 E California Blvd., Pasadena, CA 91125, USA
[3] Division of Engineering and Applied Science, California Institute of Technology, 1200 E California Blvd., Pasadena, CA 91125, USA
[4] Jet Propulsion Laboratory, California Institute of Technology, 4800 Oak Grove Dr., Pasadena, CA 91109, USA
[5] Department of Electrical Engineering and Computer Science, Massachusetts Institute of Technology, 50 Vassar St., Cambridge, MA 02139, USA
[6] John A. Paulson School of Engineering and Applied Sciences, Harvard University, 29 Oxford St., Cambridge, MA 02138, USA
[7] Fermi National Accelerator Laboratory, Batavia, IL 60510, USA
[*] Corresponding author: smaria@caltech.edu

Compiled January 25, 2022

We demonstrate real-time single photon heralding from a bulk nonlinearity using an efficient and low-noise photon-number-resolving superconducting nanowire detector. A maximum reduction of 0.118 ± 0.012 in the photon $g^2(0)$ correlation function is obtained, indicating a strong suppression of multi-photon emissions. We analytically model our experimental results using a phase-space formalism and obtain excellent agreement. Our experiment, built using fiber-coupled and off-the-shelf components, delineates a path to engineering ideal sources of single photons.

http://dx.doi.org/10.1364/ao.XX.XXXXXX

1. INTRODUCTION

A challenge in quantum optical science and technology is the realization of an ideal, i.e deterministic, high-fidelity, tunable, and high-rate, source of indistinguishable single-photons [1, 2]. One intuitive approach to develop a single-photon source requires coupling an individual quantum emitter to light using a cavity. Significant progress in this regard [3] has been achieved using e.g. quantum dots [4–6], crystal defects [7], or trapped ions [8] and atoms [9], albeit mired with challenges, including fabrication complexity [10, 11] or differing emitter spectra [12–14]. Instead, the strong light-matter coupling offered by solid-state bulk nonlinearities can be used to probabilistically emit photon pairs via laser-driven $\chi^{(2)}$ and $\chi^{(3)}$ processes [15], i.e. spontaneous parametric down-conversion (SPDC) and four-wave mixing (SFWM), respectively. Thermal statistics of the emission restrict a single photon pair to be emitted with low probability (e.g. 10^{-3} in practice [16]). An individual photon (in a signal mode) can be heralded by the detection of the other photon (in an idler mode) [1]. Typically this is performed using a threshold detector that discriminates zero from one or more photons. Heralding of photons from optical nonlinearities is scalable, and has enabled tunable and indistinguishable photons with high fidelities and bandwidths [1, 17, 18]. However, there is a non-zero probability to produce multiple pairs. To exclude these pairs, we detect the idler mode from an SPDC process *in real time* using a novel photon-number-resolving (PNR) niobium nitride (NbN) superconducting nanowire single-photon detector (SNSPD) [19]. The detector is optimized across several performance metrics [20], namely efficiency $> 70\%$, dark count rate of 10 Hz, timing resolution (jitter) of < 14 ps, and a high single-photon discrimination efficiency, defined in Sec. 3. Specifically, we perform a second-order correlation $g^2(0)$ function measurement [21] of the signal mode conditioned on the measured photon number of the idler mode using the number-resolving detector. We operate the detector in two configurations: (i) as a PNR SNSPD, discriminating zero-, one- and multi-photon events, and (ii) as a threshold SNSPD, discriminating zero-photon events from all other events. A $g^2(0)$ of zero is expected when a single photon pair is generated. We measure a maximum reduction of $g^2(0)$ from 0.430 ± 0.009 to 0.312 ± 0.008 when using configuration (ii) versus (i), thereby improving the fidelity of the single photon source. Our non-zero $g^2(0)$ is primarily due to multi-photon events and photon loss. For a fixed $g^2(0) = 7 \times 10^{-3}$, we increase the probability to generate a single pair by 25%, from 4×10^{-3} to 5×10^{-3}, which is state-of-the-art [22]. Our results are analytically modeled using a phase-space formalism based on characteristic functions that incorporate all relevant imperfections [23–25].

2. EXPERIMENTAL METHODS

The experimental setup is shown in Fig. 1. Light pulses of ~ 600 ps duration are created by injecting 1540 nm wavelength

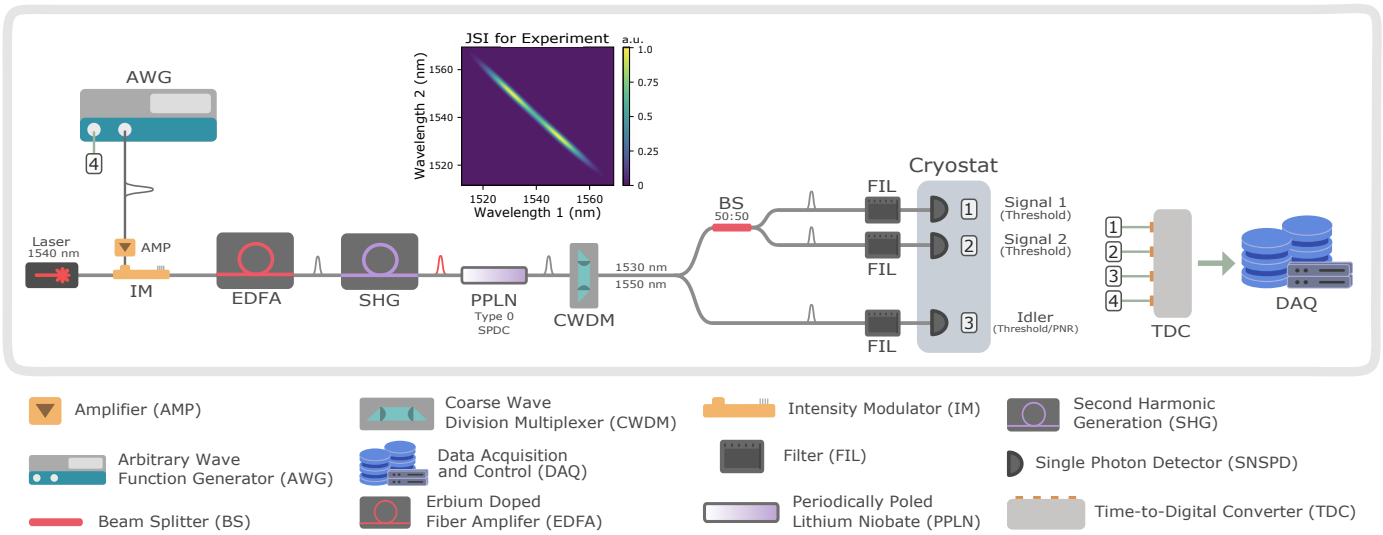

Fig. 1. Experimental setup. AWG - Tektronix AWG7002A, BS - Thorlabs 1550nm fiber optic 50:50 beamsplitter, CWDM - FS one-channel Coarse Wave Division Multiplexing/Optical Add/Drop Multiplexer, EDFA - Pritel Optical Fiber Amplifer, Laser - General Photonics TLS-101, PPLN - Covesion Ruggedized Waveguide, SHG - Pritel Optical Fiber Amplifier/Second Harmonic Generator. The inset shows the estimated joint spectral intensity (JSI) for the experiment including the detector and CWDM response.

light from a continuous-wave laser into an intensity modulator (IM). The modulator is driven by an arbitrary waveform generator (AWG) at a rate of 1 MHz, which is the clock rate of the experiment. The pulses are amplified by an erbium doped fiber amplifier (EDFA) and then directed to a second harmonic generation module (SHG), which up-converts the pulses to 770 nm. The 770 nm pulses pump a fiber-coupled type-0 periodically poled lithium niobate (PPLN) waveguide, which produces photon pairs centered at 1540 nm wavelength by way of SPDC. A coarse wavelength division multiplexer (CWDM) splits the photon pairs into the signal and idler paths, centered at 1530 nm and 1550 nm, respectively, each with a 13 nm bandwidth. The estimated joint spectral intensity (JSI) including the detector response and CWDMs is shown in Fig. 1, corresponding to a multi-mode spectrum with a Schmidt number of $K = 33.7$ (see Supplement 1) [26]. We vary the mean photon number of pairs μ by changing the input power to the SHG module. Light in the signal path is split by a 50:50 beamsplitter (BS) into two paths, labelled as signal 1 and 2. Filters with a total of 60 dB extinction on the idler path and 120 dB extinction on the signal path are used to suppress the unconverted 770 nm pump light. The photons from the signal and idler paths are detected using conventional and PNR SNSPDs, respectively. The readout pulses from the detectors and the 1 MHz signal from the AWG are sent to a time tagger, which is interfaced with custom-made software for real-time analysis and multi-photon event discrimination (see Supplement 1).

To measure the signal modes, we use two single-pixel tungsten silicide (WSi) SNSPDs, which have timing jitters of ~ 50 ps, efficiencies of $\sim 80\%$, and dark count rates below 5 Hz [16]. To measure the idler mode, we use a PNR SNSPD with an active area of 22×15 μm^2, formed by a meander of 100-nm-wide and 5-nm-thick niobium nitride (NbN) nanowires with a 500 nm pitch. The detector employs a differential architecture to cancel the contribution of the signal propagation delays to the timing jitter [19]. An impedance-matching taper enables photon-number resolution, increases the signal-to-noise ratio, and minimizes reflections as well as distortion [19, 27]. The number of incident photons is encoded in the amplitude of the output pulse [19, 28]. A single incident photon, absorbed by the nanowire, induces a single time-dependent resistive hotspot, resulting in a radio-frequency pulse [20]. Multiple incident photons that are absorbed by the nanowire at the same time induce multiple time-dependent resistive hotspots. This increases the total resistance of the nanowire, producing a radio-frequency pulse with an amplitude and slew rate that depends on the number of hotspots. In our experiments, rather than measuring the pulse amplitude variation [19, 28], we measure its slew rate variation [29]. This only requires a constant-threshold time tagger and thereby enables real-time readout. With a fixed voltage threshold, the variation in slew rate results in a variation of the registered time-tag. Earlier (later) time-tags arriving in the left (right) bin of Fig. 2 correspond to multi-photon (single-photon) pulses with higher (lower) slew rate.

3. MODEL

The second-order correlation function of photons in the signal 1 and 2 paths conditioned on the detection of the idler for the threshold and PNR configurations is calculated as

$$g^2(0) = \frac{C_{is_1s_2}C_i}{C_{is_1}C_{is_2}}, \tag{1}$$

where $C_{is_1s_2}$ is the number of threefold coincidence detection events of photons in the idler and the two signal paths, C_i is the number of idler detection events, and C_{is_j} is the number of idler and signal j twofold coincidence detection events, where $j = 1, 2$. We develop a theoretical model that takes into account full multi-photon effects, losses, and multi-mode behavior to determine the dependence of $g^2(0)$ on μ. Analytical expressions for all relevant detection rates, including twofold and threefold coincidence rates, $g^2(0)$ as a function of μ, and efficiencies are derived using a characteristic function-based approach [23]. For our experiment, we construct the symplectic transformation that maps the characteristic function of the state after the CWDMs,

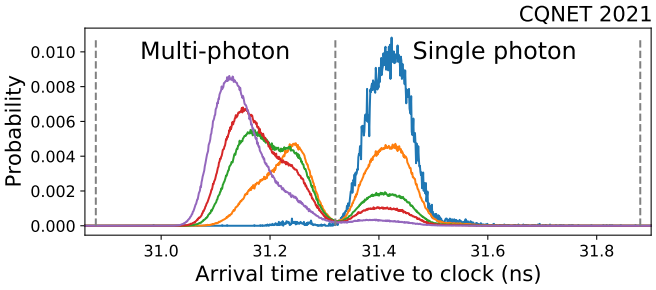

Fig. 2. Probability distribution of the arrival times of detection events by the PNR SNSPD for $\mu = 0.082 \pm 5.2 \times 10^{-4}$ (blue), $\mu = 2.8 \pm 2.7 \times 10^{-2}$ (orange), $9.1 \pm 1.3 \times 10^{-2}$ (green), $\mu = 12 \pm 1.5 \times 10^{-2}$ (red), and $\mu = 18 \pm 2.5 \times 10^{-2}$ (purple). The dashed lines define the time bins corresponding to single- (right) and multi-photon (left) events. The total number of events in the single- and multi-photon bins are used when operating the SNSPD as a threshold detector, while the number of events in the single-photon bin are used when operating the SNSPD as a PNR detector.

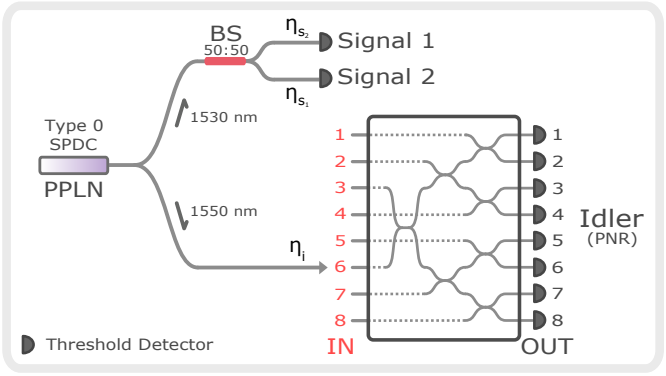

Fig. 3. Schematic of the setup used for theoretical modeling. The PNR detector is modeled as a $2N$-port beamsplitter in a binary tree architecture with threshold detectors at the outputs. See the main text for details.

which is a multi-mode squeezed vacuum state, to that of the state prior to detection. This is permitted because the states and all relevant experimental operations are Gaussian. The characteristic function is constructed using the Schmidt modes of the JSI (see Supplement 1) [30].

We calculate the detection probability using,

$$Tr[\hat{\rho}\hat{\Pi}] = \left(\frac{1}{2\pi}\right)^N \int dx^{2N} \chi_\rho(x)\chi_\Pi(-x), \tag{2}$$

where $\hat{\rho}$ describes an N-mode state prior to detection, $\hat{\Pi}$ is the measurement operator corresponding to the detector, $\chi_\rho(x)$ is the characteristic function of $\hat{\rho}$, and $\chi_\Pi(x)$ is the characteristic function of $\hat{\Pi}$. Since the measurement operators describing PNR detectors are not Gaussian operators [31], unlike threshold detectors, we cannot immediately evaluate Eq. (2) to find the detection probabilities for the PNR detector. Instead, we model the PNR detector as beamsplitter an effective $2N$-port beamsplitter with threshold detectors at each output port [24, 25, 32, 33]. We implement the $2N$-port beamsplitter as a network of beamsplitters forming a so-called "binary tree" architecture, which has N input and output ports, as shown in Fig. 3 for the case $N = 8$. To model a PNR detector, photons are injected to an input of the "top-most" beamsplitter of the tree, which corresponds to input 6 in the figure. The detection of photons with the PNR SNSPD is modeled as detection events from any combination of threshold detectors at the output ports of the tree. For an input Fock state $|n\rangle$, the probability that multiple photons arrive to the same output port is negligible when $N \gg n$, corresponding to ideal photon number discrimination. In this case, the number of detection events equals the number of input photons. For $N \sim n$, the probability of multiple photons arriving to the same output port is non-negligible, corresponding to non-ideal photon number discrimination. In this case, the number of detection events does not equal the number of input photons. Therefore, the depth of the tree $k = \log_2(N)$, is a figure of merit for photon number discrimination. A schematic of the binary tree model for $k = 3$ is shown in Fig. 3, where η_{s_1}, η_{s_2}, and η_i denote the efficiencies (including all coupling and detection losses) of the signal 1, signal 2, and idler paths, respectively. Using the schematic depicted in Fig. 3, we employ characteristic function techniques for Gaussian states to find analytical expressions for the single-photon detection probabilities of the PNR SNSPD, threshold detection probabilities of the conventional SNSPDs, and the twofold and threefold coincidence probabilities of photons in signal 1, signal 2, and idler paths, as a function of $\mu, \eta_{s_1}, \eta_{s_2}, \eta_i$, k, and the Schmidt coefficients (see Supplement 1). These expressions are then used to calculate $g^2(0)$ from Eq. (1). Moreover, we use our model to define the single-photon discrimination efficiency of the PNR detector as

$$\eta_{PNR} = \frac{P(1|1)}{\sum_{n=0}^{\infty} P(1|n)}, \tag{3}$$

where $P(1|n)$ is the probability that the detector registers a single photon given that n photons were incident on the detector. The η_{PNR} is zero for a threshold detector and one for an ideal PNR detector. For more details, see Supplement 1.

4. RESULTS

We vary μ and measure the corresponding $g^2(0)$ for configurations (i) and (ii). The results are shown in Fig. 4. We observe suppression of multi-photon events, as indicated by a reduction of $g^2(0)$. We obtain a maximum reduction of 0.118 ± 0.012, as shown in the inset of Fig. 4a. To determine μ, we fit Eq. (S59) to our measurement results using configuration (ii), and to determine k, we fit Eq. (S51) to the single photon detection rates using configuration (i). The η_{s_1}, η_{s_2} and η_i are calculated from the single and twofold coincidence detection events for $\mu < 6 \times 10^{-3}$. For our experiment, $k = 2.71$ and the detector efficiency is 0.71, which yields $\eta_{PNR} = 0.427$. Thus, the single-photon discrimination of our detector is comparable to that of a pseudo-PNR detector comprised of no more than seven threshold detectors, each with a detector efficiency of 0.71. The data used to calculate $g^2(0)$, along with the fit details, are found in Supplement 1. As seen from Fig. 4, our model agrees with the experimental results. The data for $\mu \leq 0.015$ is presented in Fig. 4b. For a $g^2(0)$ of 7×10^{-3} (black dashed line) [22], the crosses and grey lines indicate the corresponding μ using configurations (ii) and (i), respectively. We observe a 25% improvement in μ, from 4×10^{-3} (blue cross) with configuration (ii), to 5×10^{-3} (green cross) with configuration (i).

Next, we estimate the performance of our experiment with future improvements (see Sec. 5). We calculate $g^2(0)$ using the

properties of our PNR detector (purple curve) and those of a nearly ideal PNR detector (red curve) for a high-efficiency single-mode SPDC source. We assume efficiencies of $\eta_{s_1} = \eta_{s_2} = \eta_i = 0.87$, which are the product of the coupling (0.91) and detector (0.96) efficiencies from Refs. [34] and [35], respectively, and are among the best-achieved to date. With these upgrades, for a $g^2(0)$ of 7×10^{-3}, we predict an improved $\mu = 9.0 \times 10^{-3}$ (purple cross) and $\mu = 1.4 \times 10^{-2}$ (red cross) using our PNR SNSPD and a nearly ideal PNR detector, respectively.

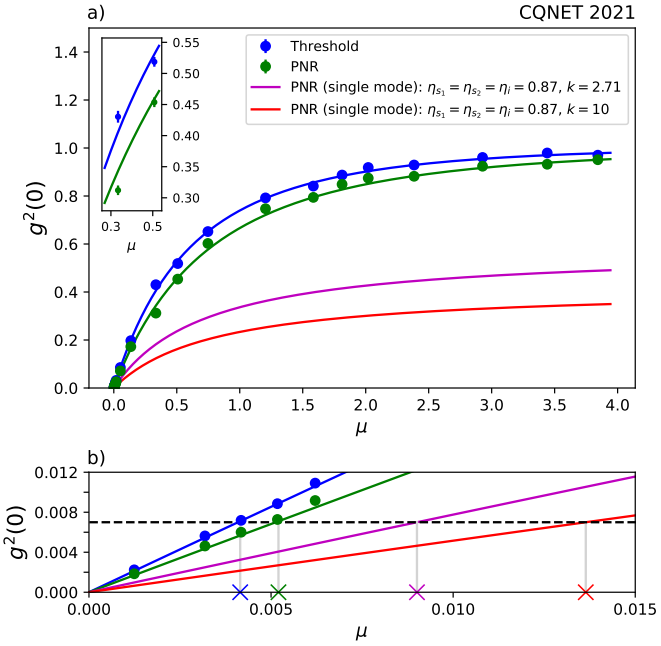

Fig. 4. a) The correlation function $g^2(0)$ with varied mean photon number for our experiment and using improved heralded single-photon sources. The data using threshold (blue) and PNR (green) configurations are represented by the circular markers. All uncertainties are calculated from Poisson statistics. The blue and green curves are obtained from the model using measured $\eta_i = 0.3280 \pm 0.0110$, $\eta_{s_1} = 0.1802 \pm 0.0063$, $\eta_{s_2} = 0.2210 \pm 0.0077$. The model predicts $k = 2.71$ for PNR detection. The inset zooms in the region where the largest reduction in $g^2(0)$ is measured. The purple and red curves are predictions using an improved source. b) The same as a) for $\mu \leq 0.015$. See main text for details.

5. DISCUSSION

By measuring the idler mode of a spontaneous parametric down-conversion source using a photon-number-resolving nanowire detector, we reduce the $g^2(0)$ of the signal mode or, on the other hand, increase the probability to generate a photon. The results and key performance metrics of our experiment are supported by a detailed analytical model which captures multi-photon effects, imperfections, and multiple spectral modes. Using a setup consisting of fiber-coupled and off-the-shelf devices, we generate photons that can be used in quantum information applications, in particular quantum communication [36, 37].

To realize an ideal single photon source [1], a number of improvements to our experiment must be implemented [38]. First, the Schmidt number of our SPDC source must be decreased from its current value of $K = 33.7$ to $K = 1$. This can be accomplished with either narrower spectral filtering of the pairs, an increase in the pump pulse bandwidth [39], the use of cavity-enhanced SPDC [40], or by engineering the phase matching function of the nonlinear crystal [41]. A near-unity Schmidt number renders the photons suitable for interference with other independently generated photons in a quantum circuit or network.

Next, the system efficiency should be increased to near unity. Coupling between fibers and devices can be improved with enhanced modal engineering [42] or using anti-reflection-coated free-space components [43]. Alternatively, components could be integrated onto the same chip, for instance using Si- or SiN-on-insulator with SFWM sources [17, 44], or using thin-film lithium niobate [45]. Furthermore, multiplexing strategies must be employed to increase the probability of generating a single pair beyond the theoretical maximum of 25% per mode. Such multiplexing, using, for instance, spatial [46, 47], temporal [34, 48], or frequency modes [49, 50], could also be employed to circumvent loss in the signal mode [51]. This requires on-demand feed-forward mode mapping using switches [52], quantum memories [53], or frequency shifters [54], respectively. Feed-forward requires the real-time readout that our PNR SNSPD allows. Multiplexing with feed-forward allows a multi-mode source to be rendered as single mode, i.e. it effectively decreases its Schmidt number to unity [50]. Our broadband SPDC source is naturally suited for frequency multiplexing, as indicated by the strong frequency correlations in our JSI [55]. This suggests our measured $\mu = 5 \times 10^{-3}$ for $g^2(0) = 7 \times 10^{-3}$ exceeds state-of-the-art SPDC sources using threshold detection, as well as quantum dots [22], accounting for multiplexing. Note that with a system efficiency of 0.87 [34, 35], and using ~ 110 multiplexed modes, the probability of our source to generate a single photon approaches unity, while maintaining a $g^2(0) = 7 \times 10^{-3}$.

Additional gains can be offered by improvements to the PNR SNSPD. A higher detector efficiency would increase the single-photon discrimination efficiency and improve the fidelity of the heralded single photon. This may be achieved through improvements to the optical stack around the nanowire by replacing the gold mirror with a distributed Bragg reflector mirror [56]. Also, the detector reset time of nearly 100 ns restricts the maximum repetition rate of the source to be ~ 10 MHz. An SNSPD with a reduced reset time based on a lower kinetic inductance nanowire material, or integrated with an active quenching circuit [57], would allow for high single-photon generation rates. A multiplexing method based on multiple PNR SNSPDs would also support a high repetition rate.

Beyond single photon sources, extensions of our setup will allow efficient generation of qubits or qudits, or entanglement swapping using PNR SNSPDs [37]. Further uses encompass preparation of heralded photon-number states [58] and non-Gaussian continuous-variable states [59], which are vital resources to realize fault-tolerant photonic quantum computers [60].

During the preparation of our manuscript we became aware of relevant results achieved independently of this work [61].

Acknowledgments. We acknowledge partial funding from the Department of Energy BES HEADS-QON Grant No. DE-SC0020376, QuantiSED SC0019219, and the AQT Intelligent Quantum Networks and Technologies (INQNET) research program. Partial support for this work was provided by the DARPA DSO DETECT, NASA SCaN and Caltech/JPL PDRDF programs. S.I.D. and A.M. acknowledge partial support from the Brinson Foundation. Part of this research was performed at the Jet Propulsion Laboratory, California Institute of Technology, under con-

tract with NASA. We acknowledge productive discussions with Kayden Taylor, Sergio Escobar, Daniel Oblak, and Cristian Peña. We are grateful to Jason Trevor for technical assistance.

See Supplement 1 for supporting content.

REFERENCES

1. M. D. Eisaman, J. Fan, A. Migdall, and S. V. Polyakov, Rev. scientific instruments **82**, 071101 (2011).
2. J. L. O'brien, A. Furusawa, and J. Vučković, Nat. Photonics **3**, 687 (2009).
3. I. Aharonovich, D. Englund, and M. Toth, Nat. Photonics **10**, 631 (2016).
4. P. Michler, A. Kiraz, C. Becher, W. Schoenfeld, P. Petroff, L. Zhang, E. Hu, and A. Imamoglu, science **290**, 2282 (2000).
5. A. J. Shields, Nanosci. And Technol. A Collect. Rev. from Nat. Journals pp. 221–229 (2010).
6. P. Senellart, G. Solomon, and A. White, Nat. nanotechnology **12**, 1026 (2017).
7. T. M. Babinec, B. J. Hausmann, M. Khan, Y. Zhang, J. R. Maze, P. R. Hemmer, and M. Lončar, Nat. nanotechnology **5**, 195 (2010).
8. H. Barros, A. Stute, T. Northup, C. Russo, P. Schmidt, and R. Blatt, New J. Phys. **11**, 103004 (2009).
9. M. Mücke, J. Bochmann, C. Hahn, A. Neuzner, C. Nölleke, A. Reiserer, G. Rempe, and S. Ritter, Phys. Rev. A **87**, 063805 (2013).
10. C. Bradac, W. Gao, J. Forneris, M. E. Trusheim, and I. Aharonovich, Nat. communications **10**, 1 (2019).
11. S. Bogdanović, M. S. Liddy, S. B. van Dam, L. C. Coenen, T. Fink, M. Lončar, and R. Hanson, APL photonics **2**, 126101 (2017).
12. D. Huber, M. Reindl, Y. Huo, H. Huang, J. S. Wildmann, O. G. Schmidt, A. Rastelli, and R. Trotta, Nat. communications **8**, 1 (2017).
13. A. Sipahigil, K. D. Jahnke, L. J. Rogers, T. Teraji, J. Isoya, A. S. Zibrov, F. Jelezko, and M. D. Lukin, Phys. review letters **113**, 113602 (2014).
14. H. Bernien, L. Childress, L. Robledo, M. Markham, D. Twitchen, and R. Hanson, Phys. Rev. Lett. **108**, 043604 (2012).
15. R. W. Boyd, *Nonlinear optics* (Academic press, 2020).
16. R. Valivarthi, S. I. Davis, C. Peña, S. Xie, N. Lauk, L. Narváez, J. P. Allmaras, A. D. Beyer, Y. Gim, M. Hussein *et al.*, PRX Quantum **1**, 020317 (2020).
17. J. Wang, F. Sciarrino, A. Laing, and M. G. Thompson, Nat. Photonics **14**, 273 (2020).
18. J. B. Spring, P. L. Mennea, B. J. Metcalf, P. C. Humphreys, J. C. Gates, H. L. Rogers, C. Söller, B. J. Smith, W. S. Kolthammer, P. G. Smith *et al.*, Optica **4**, 90 (2017).
19. M. Colangelo, B. Korzh, J. P. Allmaras, A. D. Beyer, A. S. Mueller, R. M. Briggs, B. Bumble, M. Runyan, M. J. Stevens, A. N. McCaughan *et al.*, preprint arXiv:2108.07962 (2021).
20. C. M. Natarajan, M. G. Tanner, and R. H. Hadfield, Supercond. science technology **25**, 063001 (2012).
21. R. J. Glauber, Phys. Rev. **130**, 2529 (1963).
22. F. Kaneda and P. G. Kwiat, Sci. advances **5**, eaaw8586 (2019).
23. M. Takeoka, R.-B. Jin, and M. Sasaki, New J. Phys. **17**, 043030 (2015).
24. A. Feito, J. Lundeen, H. Coldenstrodt-Ronge, J. Eisert, M. B. Plenio, and I. A. Walmsley, New J. Phys. **11**, 093038 (2009).
25. D. Achilles, C. Silberhorn, C. Sliwa, K. Banaszek, I. A. Walmsley, M. J. Fitch, B. C. Jacobs, T. B. Pittman, and J. D. Franson, J. Mod. Opt. **51**, 1499 (2004).
26. K. Zielnicki, K. Garay-Palmett, D. Cruz-Delgado, H. Cruz-Ramirez, M. F. O'Boyle, B. Fang, V. O. Lorenz, A. B. U'Ren, and P. G. Kwiat, J. Mod. Opt. **65**, 1141 (2018).
27. D. Zhu, M. Colangelo, B. A. Korzh, Q.-Y. Zhao, S. Frasca, A. E. Dane, A. E. Velasco, A. D. Beyer, J. P. Allmaras, E. Ramirez *et al.*, Appl. Phys. Lett. **114**, 042601 (2019).
28. D. Zhu, M. Colangelo, C. Chen, B. A. Korzh, F. N. Wong, M. D. Shaw, and K. K. Berggren, Nano Lett. **20**, 3858 (2020).
29. C. Cahall, K. L. Nicolich, N. T. Islam, G. P. Lafyatis, A. J. Miller, D. J. Gauthier, and J. Kim, Optica **4**, 1534 (2017).
30. K. Zielnicki, K. Garay-Palmett, D. Cruz-Delgado, H. Cruz-Ramirez, M. F. O'Boyle, B. Fang, V. O. Lorenz, A. B. U'Ren, and P. G. Kwiat, J. Mod. Opt. **65**, 1141 (2018).
31. U. Leonhardt, *Measuring the quantum state of light*, vol. 22 (Cambridge university press, 1997).
32. M. Fitch, B. Jacobs, T. Pittman, and J. Franson, Phys. Rev. A **68**, 043814 (2003).
33. H. Paul, P. Törmä, T. Kiss, and I. Jex, Phys. review letters **76**, 2464 (1996).
34. F. Kaneda, K. Garay-Palmett, A. B. U'Ren, and P. G. Kwiat, Opt. express **24**, 10733 (2016).
35. M. K. Akhlaghi, E. Schelew, and J. F. Young, Nat. communications **6**, 1 (2015).
36. H. B. Ch and G. Brassard, "Quantum cryptography: public key distribution and coin tossing int," in *Conf. on Computers, Systems and Signal Processing (Bangalore, India,* , vol. 175 (1984).
37. H. Krovi, S. Guha, Z. Dutton, J. A. Slater, C. Simon, and W. Tittel, Appl. Phys. B **122**, 52 (2016).
38. A. Christ and C. Silberhorn, Phys. Rev. A **85**, 023829 (2012).
39. J. Rarity, Annals New York academy Sci. **755**, 624 (1995).
40. T. Herzog, J. Rarity, H. Weinfurter, and A. Zeilinger, Phys. review letters **72**, 629 (1994).
41. P. J. Mosley, J. S. Lundeen, B. J. Smith, P. Wasylczyk, A. B. U'Ren, C. Silberhorn, and I. A. Walmsley, Phys. Rev. Lett. **100**, 133601 (2008).
42. B. S. Kawasaki, K. O. Hill, and R. Lamont, Opt. Lett. **6**, 327 (1981).
43. L. K. Shalm, E. Meyer-Scott, B. G. Christensen, P. Bierhorst, M. A. Wayne, M. J. Stevens, T. Gerrits, S. Glancy, D. R. Hamel, M. S. Allman *et al.*, Phys. review letters **115**, 250402 (2015).
44. J. W. Silverstone, D. Bonneau, K. Ohira, N. Suzuki, H. Yoshida, N. Iizuka, M. Ezaki, C. M. Natarajan, M. G. Tanner, R. H. Hadfield *et al.*, Nat. Photonics **8**, 104 (2014).
45. D. Zhu, L. Shao, M. Yu, R. Cheng, B. Desiatov, C. Xin, Y. Hu, J. Holzgrafe, S. Ghosh, A. Shams-Ansari *et al.*, Adv. Opt. Photonics **13**, 242 (2021).
46. M. J. Collins, C. Xiong, I. H. Rey, T. D. Vo, J. He, S. Shahnia, C. Reardon, T. F. Krauss, M. Steel, A. S. Clark *et al.*, Nat. communications **4**, 1 (2013).
47. G. J. Mendoza, R. Santagati, J. Munns, E. Hemsley, M. Piekarek, E. Martín-López, G. D. Marshall, D. Bonneau, M. G. Thompson, and J. L. O'Brien, Optica **3**, 127 (2016).
48. C. Xiong, X. Zhang, Z. Liu, M. J. Collins, A. Mahendra, L. Helt, M. J. Steel, D.-Y. Choi, C. Chae, P. Leong *et al.*, Nat. communications **7**, 1 (2016).
49. C. Joshi, A. Farsi, S. Clemmen, S. Ramelow, and A. L. Gaeta, Nat. communications **9**, 1 (2018).
50. M. G. Puigibert, G. Aguilar, Q. Zhou, F. Marsili, M. Shaw, V. Verma, S. Nam, D. Oblak, and W. Tittel, Phys. Rev. Lett. **119**, 083601 (2017).
51. N. Sinclair, E. Saglamyurek, H. Mallahzadeh, J. A. Slater, M. George, R. Ricken, M. P. Hedges, D. Oblak, C. Simon, W. Sohler *et al.*, Phys. review letters **113**, 053603 (2014).
52. P. Xu, J. Zheng, J. K. Doylend, and A. Majumdar, ACS Photonics **6**, 553 (2019).
53. A. I. Lvovsky, B. C. Sanders, and W. Tittel, Nat. photonics **3**, 706 (2009).
54. Y. Hu, M. Yu, D. Zhu, N. Sinclair, A. Shams-Ansari, L. Shao, J. Holzgrafe, E. Puma, M. Zhang, and M. Lončar, Nature **599**, 587 (2021).
55. T. Hiemstra, T. Parker, P. Humphreys, J. Tiedau, M. Beck, M. Karpiński, B. Smith, A. Eckstein, W. Kolthammer, and I. Walmsley, Phys. Rev. Appl. **14**, 014052 (2020).
56. D. V. Reddy, R. R. Nerem, S. W. Nam, R. P. Mirin, and V. B. Verma, Optica **7**, 1649 (2020).
57. P. Ravindran, R. Cheng, H. Tang, and J. C. Bardin, Opt. express **28**, 4099 (2020).
58. M. Cooper, L. J. Wright, C. Söller, and B. J. Smith, Opt. express **21**, 5309 (2013).
59. D. Su, C. R. Myers, and K. K. Sabapathy, Phys. Rev. A **100**, 052301 (2019).
60. J. E. Bourassa, R. N. Alexander, M. Vasmer, A. Patil, I. Tzitrin, T. Matsuura, D. Su, B. Q. Baragiola, S. Guha, G. Dauphinais *et al.*, Quantum **5**, 392 (2021).
61. S. Sempere-Llagostera, G. Thekkadath, R. Patel, W. Kolthammer, and

I. Walmsley, arXiv preprint arXiv:2111.15308 (2021).